

We are IntechOpen, the world's leading publisher of Open Access books Built by scientists, for scientists

6,900

Open access books available

186,000

International authors and editors

200M

Downloads

Our authors are among the

154

Countries delivered to

TOP 1%

most cited scientists

12.2%

Contributors from top 500 universities



WEB OF SCIENCE™

Selection of our books indexed in the Book Citation Index
in Web of Science™ Core Collection (BKCI)

Interested in publishing with us?
Contact book.department@intechopen.com

Numbers displayed above are based on latest data collected.
For more information visit www.intechopen.com



Nanoindentation Based Analysis of Heterogeneous Structural Materials

Jiří Němeček

Additional information is available at the end of the chapter

<http://dx.doi.org/10.5772/50968>

1. Introduction

Nanoindentation is undoubtedly a powerful experimental technique, developed for more than a decade together with new device technologies, characterization of lower scale physical laws, theories and small scale numerical modelling. Nowadays, nanoindentation (Fischer-Cripps, 2002) is commonly used for investigation of local mechanical properties of mostly homogeneous materials modelled as isotropic (Oliver & Pharr, 1992) or anisotropic solids (Swadener & Pharr, 2001; Vlassak et al., 2003). On the other hand, many materials and especially structural ones exhibit phase heterogeneity and mechanical differences of the phases on different length scales (nanometers to meters). In order to model heterogeneous material systems, multiscale approach that allows for separation of scales based on some characteristic dimension of a material microscopic feature for each level is often utilized. Material micro-level of selected structural materials whose properties are accessible by nanoindentation (below one micrometer) will be analyzed in this chapter. Phase separation based on their different mechanical behaviour and intrinsic phase properties of the selected materials will be performed. Statistical grid indentation technique will be employed (Constantinides et al., 2006; Ulm et al., 2007; Němeček et al., 2011c). Finally, micromechanical framework (Zaoui, 2002) will be applied in the analysis of the effective composite properties for higher material levels.

2. Heterogeneity of structural materials

Structural materials exhibit several types of heterogeneity at microscale. The first type of their heterogeneity comes from mixing of components that do not react chemically in the composite like sand, fibres, and other additives. Such heterogeneity is usually known in advance and is given by the mixing proportions. The second type of heterogeneity comes from chemical reactions that are evolving after the mixing of basic components. As a result

of these reactions, new phases are produced. In the case of structural materials, it is hard to rigorously define their volumes and microstructural distribution. Cement paste or alkali-activated materials can be given as typical examples. After many decades of research, exact microstructure development of these materials and the link between their basic components and their mechanical performance is still an open issue. Their microstructure is rather complex and it is, therefore, impossible to separate the phases from the composite and to prepare homogeneous-like samples suitable for mechanical testing.

Formation of the new phases in the structural composites includes fully or partly reacted matrix, unreacted grains of the raw material, interfacial zones with different chemical and also mechanical properties (e.g. Taylor, 2003; Bentz, 1999) and porosity. Structural materials based on cement (like cement paste, concrete, plasters) or waste materials (like fly-ash, furnace slag, etc.) usually include both types of the heterogeneity.

Complementary techniques to nanoindentation, such as optical imaging, electron microscopy (SEM) or atomic force microscopy (AFM) are often used to separate and to characterize the material phases. These techniques allow qualitative as well as quantitative investigation of individual material phases at small volumes near or at the sample surface. Measurement of intrinsic properties of individual material phases can be performed almost exclusively by nanoindentation that can directly access mechanical properties at small volumes starting from several tens of nanometers (depending on sample and probe). Complicated microstructures (e.g. trabecular bones, porous ceramics) are sometimes treated by a combination of nanoindentation with small scale mechanical testing (e.g. Jiroušek et al., 2011b). The microstructure of these materials can be reconstructed by X-ray microtomography in combination with the specimen loading (Jiroušek, 2011a).

The final step in the micromechanical analysis includes up-scaling of the properties to the higher material level. Multiple tools of classical analytical micromechanics or numerical approaches can be employed in this task (e.g. Zaoui, 2002; Moulinec & Suquet, 1994, 1998; Michel et al., 1999).

3. Testing strategies

In contrast to usual indentation on homogeneous materials (e.g. glass, films, coatings), structural materials (e.g. cement paste, alkali-activated materials, gypsum) are much more complex in their microstructure and mechanical performance. The situation is further complicated by their time-dependent load response (Němeček, 2009), aging and property fluctuations due to temperature or humidity (Beaudoin et al., 2010; Randall, 2009). The evaluation methodology however, is currently restricted mostly to homogeneous isotropic systems (Oliver & Pharr, 1992). The indentation response in the form of force-penetration (P - h) curves is characterized by two elastic constants, indentation modulus:

$$E_r = \frac{1}{2\beta} \frac{\sqrt{\pi}}{\sqrt{A_c}} \frac{dP}{dh} \Big|_{P=P_{\max}} \quad (1)$$

and indentation hardness:

$$H = \frac{P}{A_c} \quad (2)$$

where $\left. \frac{dP}{dh} \right|_{P=P_{\max}}$ is the contact stiffness evaluated from the initial slope of the unloading branch of the force-penetration curve, P is the indentation force, A_c is the projected contact area and β is the correction factor for indenters with non-symmetrical shape ($\beta=1.034$ for Berkovich tip). Direct application of these equations to heterogeneous materials poses several difficulties, as the underlying analysis relies on the self-similarity of the indentation test which holds only for homogeneous materials (Borodich et al., 2003; Constantinides, 2007). The interaction of phases in heterogeneous materials is unavoidable but depending on the length scale it can be more or less important. Properties extracted from indentation data of a heterogeneous solid can be treated as averaged quantities dependent on the depth h . Therefore, the choice of an indentation depth directly determines the length scale of the tested material volume. For example, the effective volume affected by an indent can be estimated as $3 \times h$ for the Berkovich indenter (Constantinides et al., 2006).

Composite structural materials are multiphase materials in which distinct phases are intermixed spatially and chemically. Taking the microstructural heterogeneity into account one can formulate basically three testing strategies to obtain mechanical properties of a composite or its phase properties:

(i) Averaged (effective) composite properties can be found if the indentation depth is much larger than the characteristic phase dimension ($h \gg D$). In this case, a phase compound is indented and thus, physically averaged properties are obtained. This strategy does not give access neither to distinct phases' properties nor to their volume fractions.

(ii) Another possibility is to perform pointed indentation to a specific material phase with individual indent's dimension much smaller than the characteristic dimension of the tested phase ($h \ll D$). In this case, intrinsic properties of the distinct phase (which may also include a phase porosity smaller than the tested size h) are obtained. This strategy can be used, provided the material phase can be distinguished prior to indentation by some other means (e.g. optical microscope, SEM) which is not always the case. It gives access to the distinct phase properties but not to volume fraction of the phase compared to other phases.

(iii) The last one, but for structural materials probably the most powerful technique, is based on the statistical (massive grid) indentation in which small indents are produced over a large area to capture the sample heterogeneity, but the dimension of a single indent is kept still smaller than the characteristic dimension of an individual phase ($h \ll D$). In this case, the results provide information on all phases' properties as well as their volume ratios, but without any knowledge which indent belongs to which phase. The properties can be evaluated in terms of property histograms for which subsequent deconvolution techniques can be employed and individual phase properties assessed (Constantinides et al., 2006; Ulm et al., 2007; Němeček et al., 2011c).

The extraction of material properties of a heterogeneous system from nanoindentation in cases of (ii) and (iii) relies on the fact that the volume affected by an indenter is small enough not to mechanically interact with other phases. As a rule of a thumb, the indentation depth is usually chosen as 1/10 of the characteristic size of the measured inclusion or phase D (Durst, 2004). In the literature, the solution of a mutual influence in the matrix-inclusion system is rather rare. The situation of phases with different stiffness was studied for thin films placed on a substrate e.g. by Gao et al., 1992. It was shown by Gao et al. that the substrate effects are negligible if the stiffness mismatch ratio is:

$$\frac{E_{\text{substrate}}}{E_{\text{film}}} \in (0.2; 5) \quad (3)$$

as long as the indentation depth is smaller than 10% of the film thickness. The layered substrate-film system is not completely equivalent to the disordered structural multiphase materials but it can be successfully used as the first estimate.

Applying (ii) strategy to cement paste, for example, where calcium-silica-hydrates of different densities (low and high) are intermixed with $Ca(OH)_2$ zones in hydrated cement matrix (Taylor, 2003; Thomas et al., 1998) is not an option due to impossible differentiation of the reaction products in optical microscope or SEM. Therefore, it is advantageous to perform massive grids (hundreds of indents) on large sample area containing all material phases. Then, the indentation offers statistical set of data which can be analyzed by the deconvolution technique (Ulm et al., 2007; Němeček, 2011c).

4. Identification of intrinsic phase properties by the deconvolution procedure

It is assumed in the algorithm that a large statistical set of independent events (i.e. measurements of elastic modulus or hardness at individual material points) is obtained from grid nanoindentation, i.e. by applying the (iii) testing strategy from the previous section. The analysis begins with the generation of experimental probability density function (PDF) or cumulative distribution function (CDF) for the data set. Using of PDF is more physically intuitive since significant peaks associated with mechanically distinct phases can be often distinguished in the graph. On the other hand, the construction of PDF requires the choice of a bin size. Application of CDF (Ulm et al., 2007) is more straightforward (does not require the choice of a bin size) and is more appropriate for cases where no clear peaks occur in the property histogram. The deconvolution algorithms based on PDF or CDF are analogous and thus the procedure will be explained just for the case of PDF.

Experimental PDF is firstly constructed from all measurements whose number is N^{exp} , using equally spaced N_{bins} bins of the size b . Each bin is assigned a frequency of occurrence f_i^{exp} that can be normalized with respect to the overall number of measurements as $\frac{f_i^{\text{exp}}}{N^{\text{exp}}}$. From

that, one can compute the experimental probability density function (PDF) as a set of discrete values:

$$p_i^{\text{exp}} = \frac{f_i^{\text{exp}}}{N^{\text{exp}}} \frac{1}{b} \quad i = 1, \dots, N_{\text{bins}} \quad (4)$$

The task of deconvolution into M phases represents finding of $r=1, \dots, M$ individual distributions related to single material phase. Assuming normal (Gauss) distributions, the single phase PDF can be written as:

$$p_r(x) = \frac{1}{\sqrt{2\pi s_r^2}} \exp\left(-\frac{(x - \mu_r)^2}{2s_r^2}\right) \quad (5)$$

in which μ_r and s_r are the mean value and standard deviation of the r -th phase computed from n_r values as:

$$\mu_r = \frac{1}{n_r} \sum_{k=1}^{n_r} x_k \quad s_r^2 = \frac{1}{n_r - 1} \sum_{k=1}^{n_r} (x_k - \mu_r)^2 \quad (6)$$

and x is the approximated quantity (i.e. elastic modulus or hardness). The overall PDF constructed from M phases is then:

$$C(x) = \sum_{r=1}^M f_r p_r(x) \quad (7)$$

where f_r is the volume fraction of a single phase defined as:

$$f_r = \frac{n_r}{N^{\text{exp}}} \quad (8)$$

Individual distributions can be found by minimizing the following error function:

$$\min \sum_{i=1}^{N_{\text{bins}}} [(P_i^{\text{exp}} - C(x_i)) P_i^{\text{exp}}]^2 \quad (9)$$

in which quadratic deviations between experimental and theoretical PDFs are computed in a set of discrete points. The function is weighted by the experimental probability in order to put emphasis on the measurements with a higher occurrence. The minimization in Eq. 9 can be based on the random Monte Carlo generation of M probability density functions satisfying the condition:

$$\sum_{r=1}^M f_r = 1 \quad (10)$$

As mentioned above, the bin size needs to be chosen prior the computation. Also, it is beneficial to fix the number of mechanically distinct phases M in advance to minimize the

computational burden and to stabilize the ill-posed problem (Němeček et al., 2011c). Such knowledge can be supplied by some independent analyses (chemical composition, SEM or image analyses).

5. Assessment of effective material properties

5.1. Analytical homogenization methods

Continuum micromechanics will serve as fundamental tool in our assessment of effective material properties. A material is considered as macroscopically homogeneous with microscopically inhomogeneous phases that fill a representative volume element (RVE) with characteristic dimension l . The scale separation condition requires to be $d \ll l \ll D$, where d stands for a size of the largest microlevel inhomogeneity in the RVE (e.g. particles or phases), l is the RVE size and D stands for structural dimension of a macroscopically homogeneous material which can be continuously built from the RVE units. The characteristic structural dimension is usually at least 4-5 times larger than the RVE size (Drugan & Willis, 1996).

The RVE with substantially smaller dimensions than the macroscale body allows imposing homogeneous boundary conditions over the RVE (Hill, 1963, 1965; Hashin, 1983). Then, continuum micromechanics provides a framework, in which elastic properties of heterogeneous microscale phases are homogenized to give overall effective properties of the upper scale (Zaoui, 2002). A significant group of analytical homogenization methods relies on the Eshelby's solution (Eshelby, 1957) that uses an assumption of the uniform stress field in an ellipsoidal inclusion embedded in an infinite body. Effective elastic properties are then obtained through averaging over the local contributions. The methods are bounded by rough estimates based on the mixture laws of Voigt (parallel configuration of phases with perfect bonding) and Reuss (serial configuration of phases). The bounds are usually quite distant so that more precise estimates need to be used. Very often, the Mori-Tanaka method (Mori & Tanaka, 1973) is used for the homogenization of composites with continuous matrix (reference medium) reinforced with spherical inclusions. In this method, the effective bulk and shear moduli of the composite are computed as follows:

$$k_{eff} = \frac{\sum_r f_r k_r (1 + \alpha_0 (\frac{k_r}{k_0} - 1))^{-1}}{\sum_r f_r (1 + \alpha_0 (\frac{k_r}{k_0} - 1))^{-1}} \quad \mu_{eff} = \frac{\sum_r f_r \mu_r (1 + \beta_0 (\frac{\mu_r}{\mu_0} - 1))^{-1}}{\sum_r f_r (1 + \beta_0 (\frac{\mu_r}{\mu_0} - 1))^{-1}}$$

$$\alpha_0 = \frac{3k_0}{3k_0 + 4\mu_0}, \beta_0 = \frac{6k_0 + 12\mu_0}{15k_0 + 20\mu_0} \quad (11)$$

where f_r is the volume fraction of the r^{th} phase, k_r is its bulk modulus, μ_r is its shear modulus, and the coefficients α_0 and β_0 describe bulk and shear properties of the 0th phase, i.e. the

reference medium (Mori & Tanaka, 1973). The bulk and shear moduli can be directly linked with Young's modulus E and Poisson's ratio ν used in engineering computations as:

$$E = \frac{9k\mu}{3k + \mu} \quad \nu = \frac{3k - 2\mu}{6k + 2\mu} \quad (12)$$

Materials with no preference of matrix phase (i.e. polycrystalline metals) are usually modeled with the self-consistent scheme (Zaoui, 2002). It is an implicit scheme, similar to Mori-Tanaka method, in which the reference medium points back to the homogenized medium itself.

5.2. Numerical homogenization based on FFT

The homogenization problem, i.e. finding the link between microscopically inhomogeneous strains and stresses and overall behavior of a RVE can be solved e.g. by finite element calculations or by applying advanced numerical schemes that solve the problem using fast Fourier transformation (FFT), for example. The later was found to be numerically efficient in connection with grid indentation that serves as a source of local stiffness parameters in equidistant discretization points. The behavior of any heterogeneous material consisting of periodically repeating RVE occupying domain Ω can be described with differential equations with periodic boundary conditions and prescribed macroscopic load ($\boldsymbol{\varepsilon}^0$) as

$$\boldsymbol{\sigma}(\mathbf{x}) = \mathbf{L}(\mathbf{x}) : \boldsymbol{\varepsilon}(\mathbf{x}) \quad \text{div} \boldsymbol{\sigma}(\mathbf{x}) = \mathbf{0} \quad \mathbf{x} \in \Omega \quad (13)$$

$$\langle \boldsymbol{\varepsilon} \rangle := \frac{1}{|\Omega|} \int_{\Omega} \boldsymbol{\varepsilon}(\mathbf{x}) d\mathbf{x} = \boldsymbol{\varepsilon}^0 \quad (14)$$

where $\boldsymbol{\sigma}(\mathbf{x})$ denotes second order stress tensor, $\boldsymbol{\varepsilon}(\mathbf{x})$ second order strain tensor and $\mathbf{L}(\mathbf{x})$ the fourth order tensor of elastic stiffness at individual locations \mathbf{x} . The effective (homogenized) material tensor \mathbf{L}_{eff} is such a tensor satisfying

$$\langle \boldsymbol{\sigma} \rangle = \mathbf{L}_{\text{eff}} \langle \boldsymbol{\varepsilon} \rangle \quad (15)$$

Local strain tensor can be decomposed to homogeneous (macroscopic) and fluctuation parts which leads to the formulation of an integral (Lippmann–Schwinger type) equation:

$$\boldsymbol{\varepsilon}(\mathbf{x}) = \boldsymbol{\varepsilon}^0 - \int_{\Omega} \Gamma^0(\mathbf{x} - \mathbf{y}) : (\mathbf{L}(\mathbf{y}) - \mathbf{L}^0) : \boldsymbol{\varepsilon}(\mathbf{y}) d\mathbf{y} \quad (16)$$

where Γ^0 stands for a periodic Green operator associated with the reference elasticity tensor \mathbf{L}^0 which is a parameter of the method (Moulinec & Suquet, 1998). The problem is further discretized using trigonometric collocation method (Saranen & Vainikko, 2002) which leads to the assemblage of a nonsymmetrical linear system of equations. The system can be resolved e.g. by the conjugate gradient method as proposed by Zeman et al. (Zeman et al., 2010). Elastic constants received from grid nanoindentation have been used as input parameters for this FFT homogenization with the assumption of plane strain conditions.

6. Experimental program

6.1. Sample preparation and microstructure

6.1.1. Cement paste

Typical heterogeneous structural materials were selected to illustrate the methodology described in previous sections. Firstly, effective elastic properties were studied for cement paste which is a basic component of a wide range of cementitious composites. Cement paste (i.e. hydrated cement clinker in hardened state) was prepared from Portland cement CEM-I 42,5 R (Mokrá, CZ) with water to cement weight ratio equal to 0.5 (Němeček, 2009). Samples were stored in water for two years. Once the cement powder is mixed with water, an exothermic reaction leading to the development of hydration products begins. The reaction kinetics is very rapid in early minutes and hours but slows down significantly after days. After a year, high degree of hydration (over 90%) could be anticipated in the samples. The microstructure of cement paste after hydration includes several major chemical phases, namely calcium-silica hydrates (C-S-H), calcium hydroxide $\text{Ca}(\text{OH})_2$ called Portlandite, residual clinker and porosity. The cement paste microstructure is shown in Fig. 1. Very light areas in Fig. 1 can be attributed to the residual clinker, light grey areas are rich of Portlandite, dark grey zone belongs to C-S-H gels and black colour represents very low density regions or capillary porosity. Note, that C-S-H gel and Portlandite zones are spatially intermixed in small volumes ($\ll 10 \mu\text{m}$) and the resolution of SEM-BSE images does not allow for a direct separation of these phases from the image.

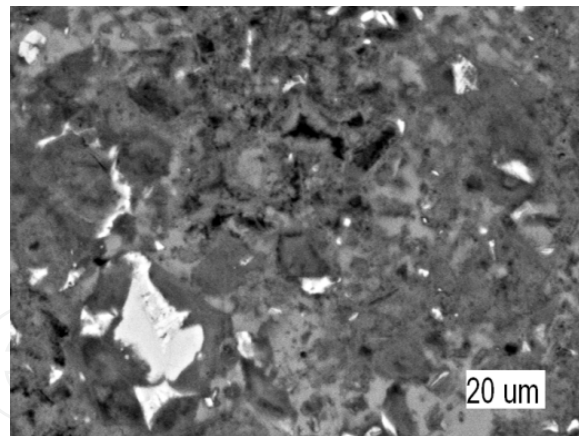


Figure 1. SEM image of cement paste microstructure.

The majority of the material volume mostly consists of poorly crystalline or amorphous phases (C-S-H) and partly of crystalline phases (Portlandite). Portlandite crystals are known for their anisotropy. Since their volume is not large in the sample and they can be mixed with C-S-H, all the phases will be supposed to be mechanically isotropic for simplification in the analysis.

Cement paste includes also wide distribution of pores. The He/Hg-porosimetry have been performed on the samples (Fig. 2). Majority of pores lies in nanometer range ($<100 \text{ nm}$) and,

on the other hand, large capillary pores are present in the scale above the indentation level (i.e. $\gg 1 \mu\text{m}$, not seen by the He/Hg-porosimetry). Therefore, the indentation depth was chosen so that the nanoporosity was included in the tested volume but the large capillary porosity was not. The depth range 100-400 nm was suitable for the analysis.

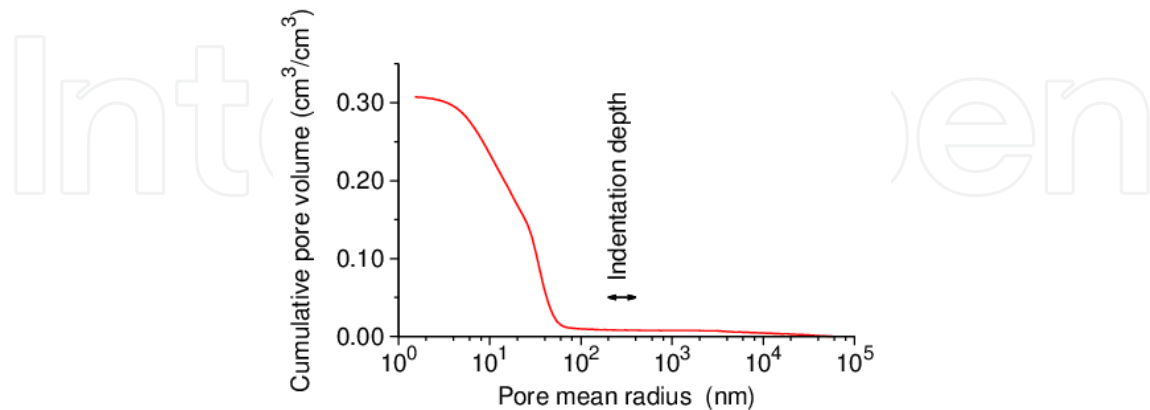


Figure 2. Cumulative pore volume on cement paste samples.

Samples for nanoindentation testing were cut from larger volume by a diamond saw and polished on series of SiC papers and diamond spray to achieve flat surface on a $\sim 5 \text{ mm}$ thick disk with diameter $\sim 30 \text{ mm}$. The surface roughness was checked with AFM to be $R_q \sim 10 \text{ nm}$ on $50 \times 50 \mu\text{m}$ area.

6.1.2. Gypsum

Secondly, dental gypsum (Interdent® Interrock New) was chosen as a model system for gypsum based materials (Tesárek & Němeček, 2010). From the chemistry point of view, every gypsum binder is composed of three main components – calcium sulphate anhydrite (CaSO_4), calcium sulphate hemihydrate ($\text{CaSO}_4 \cdot \frac{1}{2}\text{H}_2\text{O}$) in two modifications: α - or β -hemihydrate, and calcium sulphate dihydrate ($\text{CaSO}_4 \cdot 2\text{H}_2\text{O}$). The gypsum binder consists also some impurities and additives in case of natural sources. The Interdent® gypsum is a low-porosity purified α -hemihydrate used for dental purposes.

From the micromechanics point of view, gypsum samples can be viewed as porous polycrystalline materials that are characterized with a macroscopically compact solid. The microstructure of the polished cross-section of the dental gypsum sample as seen in electron microscope is shown in Fig. 3. Dark areas in Fig. 3 can be attributed to the porosity, very light areas belong to low hydrated CaSO_4 grains or carbonates and the majority of the sample volume composes of hydrated crystalline mass.

Samples were prepared with water to binder weight ratio 0.2 and stored in ambient conditions for 20 days (full strength occurs after a day). After mixing, the material begins to crystallize with maximum heat development in the order of minutes. The hardened gypsum mass is a porous material with a relatively large internal surface consisting of interlocking crystals in the form of plates and needles (Singh & Middendorf, 2007). In case of β -

hemihydrate hydration, the resulting sample porosity is typically very large (more than 50% for higher water to binder ratios) and crystals are interlocked very weakly. Therefore, ordinary gypsum systems used for building purposes which are based on β -hemihydrate are characterized with relatively low strengths (<10 MPa in compression). In contrast, hydration of our samples based on α -hemihydrate produced a dense matrix. Overall sample porosity reached just 19% as assessed by sample weighing. Since pore system plays a key mechanical role in gypsum materials, the pore distribution was monitored with Hg-porosimetry (MIP) as depicted in Fig. 4. The majority of pores lay in the range 0-1 μm (~12%) and virtually no pores appeared between 1 and 100 μm (<0.5%). The MIP technique does not allow to access large capillary/entrapped air porosity. It means that ~7% of pores was not accessible by MIP and can be attributed to large air voids.

Again, the indentation depth was chosen so that major nanoporosity was included in the tested volume whereas large air porosity was not. The indentation depths ~500 nm (i.e. $(3 \times 0.5)^3 = 1.5^3 \mu\text{m}^3$ tested volume) were chosen as suitable for the analysis.

For nanoindentation testing, samples were cut and polished in the same way like cement paste to receive ~5 \times 30 mm disk with a flat surface. The surface roughness checked with AFM was $R_q \approx 40$ nm on 50 \times 50 μm area.

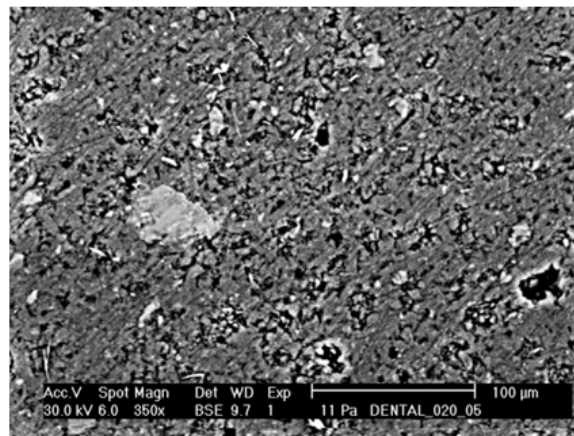


Figure 3. SEM image of gypsum.

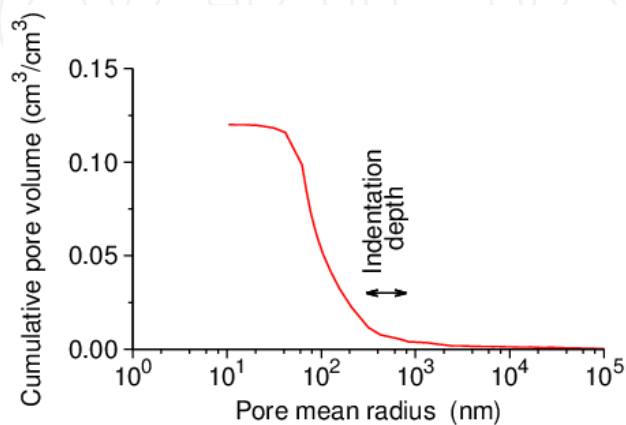


Figure 4. Cumulative pore volume on gypsum samples.

6.2. Grid nanoindentation

6.2.1. Cement paste

Nanoindentation measurements were performed in a load control regime using the CSM Nanohardness tester in the Micromechanics laboratory of the Czech Technical University in Prague. The trapezoidal loading diagram was prescribed for all tests (Fig. 5). Maximum force 2 mN was applied with constant load rate 12 mN/min. The loading lasted for 10 s. The holding period, in which the load was kept constant for 30 s, followed, allowing the material to creep (Němeček, 2009). The following unloading branch of 12 mN/min for 10 s was supposed to be purely elastic. The applied maximum load of 2 mN led to maximum penetration depths ranging from 100 nm to 400 nm (average 220 nm) depending on the hardness of the indented material phase.

The effective depth captured by the tip of the indenter can be roughly estimated as three times the penetration depth for the Berkovich indenter (Constantinides et al., 2006). It yields the affected volume of around $\sim 0.7^3 \mu\text{m}^3$ for this particular case. Nanoindentation response obtained for different material constituents is depicted in Fig. 5 and it clearly shows different deformations and stiffness of distinct phases if the same load is applied. Elastic properties were evaluated from nanoindentation tests according to the Oliver-Pharr methodology (Oliver & Pharr, 1992).

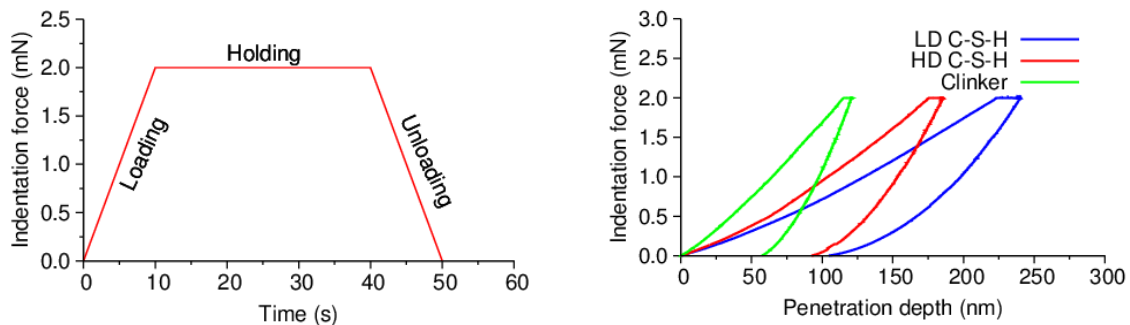


Figure 5. Prescribed loading diagram and examples of force-penetration curves for different cement paste constituents.

Due to the heterogeneity of the sample and uneven distribution of the phases in its volume, the results from individual indentation grids depend very much on the location and indents' spacing. As observed in SEM, the heterogeneity occurs on the scale of tens or even hundreds of μm (Němeček, 2009). This fact leads to the necessity to cover relatively large areas of the sample by large grids. Several sample locations containing the material phases in a sufficient content ($\sim 100 \times 100$ to $200 \times 200 \mu\text{m}$ with $10\text{-}20 \mu\text{m}$ spacing) have been performed on the sample.

Results from ~ 400 indents have been obtained on the sample and Young's moduli evaluated from individual locations (assuming Poisson's ratio 0.2 for all phases). Results were merged and property histograms constructed. The experimental histogram covers all these material phases including their intrinsic nanoporosity. According to the cement chemistry, the phases can be denoted as:

- Low stiffness phase (all phases with Young's modulus less than ~ 10 GPa)
- Low density C-S-H (i.e. C-S-H gel with loose packing density)
- High density C-S-H (i.e. C-S-H gel with high packing density)
- Portlandite $\text{Ca}(\text{OH})_2$
- Clinker residue

The deconvolution into the mechanically distinct phases that correspond to the aforementioned chemical phases (A-D) has been carried out with the assumption that values of Young's modulus higher than ~ 50 GPa can be attributed to residual clinker grains (E) and were not considered in the deconvolution because of very low content. Instead, separate 'ex-situ' measurements of clinker stiffness were performed (Němeček, 2009). The reason for the separate clinker measurements was twofold. The first reason lies in the low clinker content and the second reason is a very high stiffness contrast to other phases which is more than 5 (Eq. 3). Due to phase interactions, the clinker stiffness is underestimated in 'in-situ' measurements.

Experimental histogram and the deconvolution of phases on cement paste are depicted in Fig. 6. Elastic constants for individual phases with their volume fractions are summarized in Tab. 1.

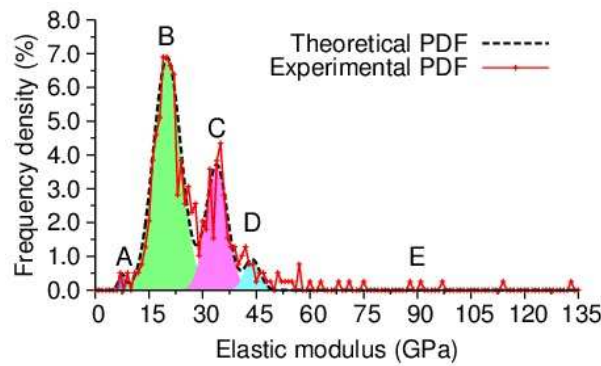


Figure 6. Deconvolution of the experimental histogram of Young's moduli to distinct material phases of cement paste.

Phase	E (GPa)	Volume fraction
Low stiffness (A)	7.45 ± 0.98	0.0105
Low density C-S-H (B)	20.09 ± 3.85	0.6317
High density C-S-H (C)	33.93 ± 2.98	0.2634
$\text{Ca}(\text{OH})_2$ (D)	43.88 ± 2.15	0.0461
Clinker (E)	$121.0 \pm 14.0^*$	0.0483

*Note: The clinker value was adjusted according to (Němeček, 2009).

Table 1. Phase properties from deconvolution on cement paste.

6.2.2. Gypsum

Similar experimental setup as for cement paste samples was used. Two locations were tested on gypsum samples. Each place was covered by $15 \times 12 = 180$ indents with $15 \mu\text{m}$ spacing.

Also, similar loading was used (i.e. load controlled test) but to maximum force 5 mN. Typical loading diagrams received on gypsum samples are depicted in Fig. 7. A bit wider range of final depths on indented phases (200-800 nm) was obtained due to larger differences in the polycrystalline stiffness. However, the majority of indents were performed to final depths ranging between 400 to 500 nm. Thus, the material volume affected by indentation can be estimated as $(3 \times 0.5)^3 = 1.5^3 \mu\text{m}^3$. The RVE size defined by the tested area is $\sim 200 \mu\text{m}$ in this case.

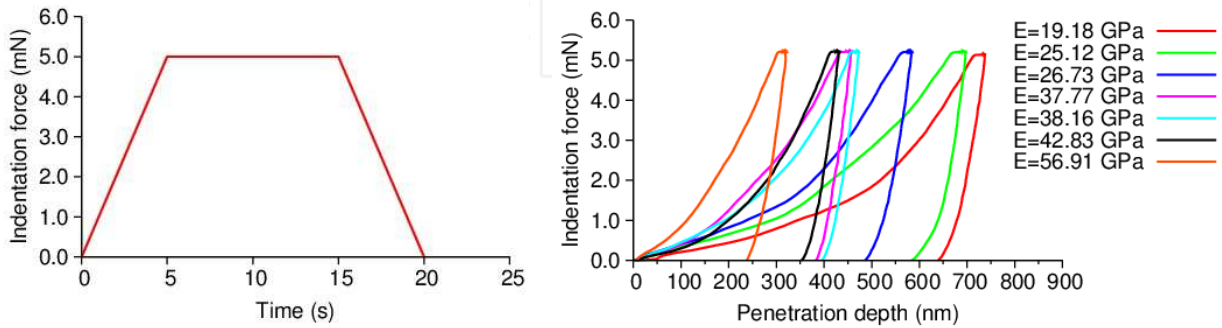


Figure 7. Prescribed loading diagram and examples of force-penetration curves at different locations on gypsum sample.

Again, results of Young's moduli (assuming Poisson's ratio 0.32), evaluated from all positions, were merged and property histogram constructed. The phase separation is not straightforward in this case, since the anisotropic gypsum crystals are squeezed in a dense polycrystalline matrix with random orientations. The response in nanoindentation is then measured on differently oriented crystals and also on a combination of differently oriented crystals located under the indenter in the affected volume $\sim 1.5^3 \mu\text{m}^3$. The tested location can be viewed as a set of mechanically different phases that are physically averaged by an indenter. Apparent isotropic elasticity constants associated with the tested indentation volume are derived in this case.

Further, it is possible to hypothesize on the number of mechanically dissimilar groups of responses from the experimental frequency plot (Fig. 8). For example, three significant peaks related to the three symmetry axes of the gypsum crystal (monoclinic system) is one of the options. Deconvolution methodology can be used to separate the three phase distributions. One can also compute apparent elastic moduli of an isotropic solid from all responses in an ensemble (i.e. compute average value from all results). Both approaches have been tested and compared.

The numerical error (Eq. 9) of the two fits was very similar and they can both be treated as numerically equivalent. Resulting phase distributions are depicted in Fig. 8. The homogenized response computed from the three-phase fit by analytical homogenizations was also mechanically equivalent to the single phase fit ($E_{(3\text{-phases})} \approx 33 \text{ GPa}$, not shown here).

Therefore, the apparent Young's modulus of a single isotropic phase will be further used as effective stiffness of already physically homogenized gypsum matrix located in the tested RVE ($\sim 200 \mu\text{m}$). This effective Young's modulus was found to be $33.90 \pm 10 \text{ GPa}$ (Fig. 8, right).

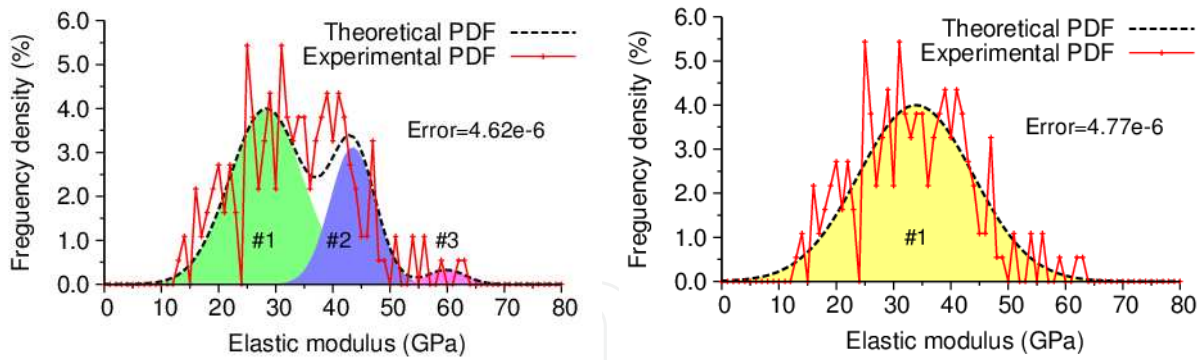


Figure 8. Experimental histogram of Young's moduli with the three-phase (left) and single-phase (right) Gaussian fits on gypsum.

7. Effective elastic properties

7.1. Cement paste

Two-scale micromechanical model was considered for cement paste. The majority of the specimen volume is occupied by C-S-H phases (in two significant densities) reinforced with nanocrystalline Portlandite particles (Thomas et al., 1998; Tennis & Jennings, 2000). Therefore, the first level of the model with the RVE size $\sim 1 \mu\text{m}$ was considered. Effective elastic constants of the first level were obtained by analytical homogenization. Low density C-S-H phase (i.e. the phase with the highest frequency) was considered as the reference phase in the Mori-Tanaka method. Analytical estimates (Mori-Tanaka and self-consistent) are shown in Tab. 3. They both give very similar results bounded with very close Voigt and Reuss limits. The Mori-Tanaka result is considered in further computations.

The second level of the micromechanical model consisted of the homogenized C-S-H phase, Portlandite, low stiffness phase and clinker. Such arrangement defined the RVE size $\sim 100 \mu\text{m}$ which corresponds to the size of indentation grids. The same analytical estimates were computed (Tab. 4).

Input	E (GPa)	Poisson's ratio	Volume fraction
Low density C-S-H (B)	20.09	0.2	0.6317
High density C-S-H (C)	33.93	0.2	0.2634
Output (B+C)			
Mori-Tanaka	23.36		
self-consistent	23.41	0.2	
Voigt bound	24.16		
Reuss bound	22.83		

Table 2. Analytical homogenization of the C-S-H level in cement paste.

Input	E (GPa)	Poisson's ratio	Volume fraction
C-S-H level (B+C)	23.36	0.2	0.8951
Low stiffness (A)	7.45	0.2	0.0105
Ca(OH) ₂ (D)	43.88	0.3	0.0461
Clinker (E)	121.00	0.3	0.0483
Output			
Mori-Tanaka	25.39	0.207	
self-consistent	25.47	0.208	
Voigt bound	29.05	0.234	
Reuss bound	24.29	0.204	

Table 3. Analytical homogenization of the cement paste level.

Results of the analytical homogenization were checked with independent FFT-based method which takes into account all indents in a grid. Elastic constants in individual grid points are considered as input values related to one discretization point in the method. The homogenized result in the form of a stiffness matrix (in Mandel's notation) of cement paste was:

$$\mathbf{L}_{\text{eff}}^{\text{FFT}} = \begin{bmatrix} 26.177 & 6.778 & 0.068 \\ 6.778 & 26.224 & 0.014 \\ 0.068 & 0.014 & 19.818 \end{bmatrix} \text{ (GPa)} \quad (17)$$

The off-axis terms in the matrix are almost zero which shows on isotropic character of the material. The result is directly comparable with the analytical result by assuming plane strain stiffness matrix for an isotropic material. Results from the Mori-Tanaka homogenization on cement paste level ($E=25.37$ GPa, $\nu=0.207$) give:

$$\mathbf{L}_{\text{eff}}^{\text{A}} = \frac{E}{(1+\nu)(1-2\nu)} \begin{bmatrix} 1-\nu & \nu & 0 \\ \nu & 1-\nu & 0 \\ 0 & 0 & 1-2\nu \end{bmatrix} = \begin{bmatrix} 28.44 & 7.43 & 0 \\ 7.43 & 28.44 & 0 \\ 0 & 0 & 21.02 \end{bmatrix} \text{ (GPa)} \quad (18)$$

The difference between the estimates can be computed by the matrix error norm:

$$\delta = \sqrt{\frac{(\mathbf{L}_{\text{eff}}^{\text{FFT}} - \mathbf{L}_{\text{eff}}^{\text{A}}) :: (\mathbf{L}_{\text{eff}}^{\text{FFT}} - \mathbf{L}_{\text{eff}}^{\text{A}})}{(\mathbf{L}_{\text{eff}}^{\text{FFT}} :: \mathbf{L}_{\text{eff}}^{\text{FFT}})}} \approx 0.08 \quad (19)$$

The 8% error shows good agreement of the methods and also near to isotropic nature of the cement paste.

7.2. Gypsum

As discussed earlier, the gypsum can be viewed as a composition of polycrystalline matrix and pore space. Therefore, two-scale micromechanical model can be defined for the gypsum sample. The lower level (i.e. the crystalline matrix) was studied by nanoindentation and effective isotropic properties were directly assessed as an average value ($E=33.90$ GPa, $\nu=0.32$) for RVE ~ 200 μm . This level also includes intrinsic porosity which is naturally included in the nanoindentation results received from the affected volume $\sim 1.5^3$ μm^3 . This part of the porosity was determined by MIP to be 12%.

The assumption of effective properties on the matrix level was checked with the FFT-based homogenization by using elastic constants measured with nanoindentation in grid points as input. The homogenized stiffness matrix (in Mandel's notation) for the lower level is:

$$\mathbf{L}_{\text{eff}}^{\text{FFT}} = \begin{bmatrix} 45.302 & 21.185 & 0.101 \\ 21.185 & 45.497 & -0.008 \\ 0.101 & -0.008 & 24.396 \end{bmatrix} \text{ (GPa)} \quad (20)$$

Comparison with the result received from nanoindentation ($E=33.90$ GPa, $\nu=0.32$) using Eq. 18 gives:

$$\mathbf{L}_{\text{eff}}^{\text{NI}} = \begin{bmatrix} 48.51 & 22.84 & 0 \\ 22.84 & 48.51 & 0 \\ 0 & 0 & 25.69 \end{bmatrix} \text{ (GPa)} \quad (21)$$

The difference between the results computed by the matrix error norm (Eq. 19) yields $\delta=0.07$, i.e. 7%. Again, very good agreement between the results from different methods was achieved.

The upper model level (the sample level) includes the first level and a part of the sample porosity that is above the indentation level which was 7% (see section 6.1.2). Therefore, micromechanical homogenization was performed for the second level assuming additional 7% porosity. Several order of magnitude smaller stiffness ($E=0.0001$ GPa) compared to the matrix was prescribed to spherical air inclusions. Naturally, Voigt and Reuss bound are very distant in this case since the first represents parallel phase configuration and the second serial configuration which in case of one almost zero stiffness phase (the air) leads to almost zero composite stiffness. The real situation in the composite (matrix reinforced with spherical air inclusions) is better described with the Mori-Tanaka method. For the sake of comparison, the self-consistent scheme was also used. It yielded a similar result for the specific case. The results are summarized in Tab. 5.

8. Discussion

It has been shown that the grid indentation and the deconvolution give access to intrinsic properties of individual material phases that are mechanically dissimilar. Both analytical and numerical schemes used for homogenization on cement paste and gypsum resulted in very similar values of elastic constants. The estimated overall elastic moduli of cement paste

Method	E (GPa)	Poisson's ratio
Mori-Tanaka	29.46	0.31
self-consistent	29.14	0.31
Voigt bound	31.52	0.32
Reuss bound	0.0014	0.49

Table 4. Results of analytical homogenization on gypsum (the sample level).

($E=25.37$ GPa) are in good agreement with those experimentally measured on larger material volumes. For example, similar values of Young's modulus can be found for the hydrated compound of cement paste in the literature, e.g. $E\sim 26.4\pm 1.8$ GPa (Němeček, 2009), $E\sim 22.8\pm 0.5$ GPa (Constantinides & Ulm, 2007; Constantinides & Ulm, 2004) or $E\sim 26.5$ GPa (Hughes & Trtik, 2004).

Since the gypsum crystallizes in the monoclinic system, the elastic stiffness tensor contains 13 nonzero components. The measurement of these constants has been performed with acoustic measurements by Haussühl, 1960. Computation of an angular average from the elastic moduli tensor leads to an isotropic stiffness $E\sim 45.7$ GPa and $\nu=0.33$ (Meille and Garboczi, 2001). Sanahuja et al. elaborated a modified self-consistent scheme for elongated gypsum crystals and computed their equivalent isotropic stiffness $E\sim 45$ GPa and $\nu=0.33$ found for zero crystal porosity. If an inter-crystalline porosity $\phi=0.2$ was taken into account the isotropic stiffness decreased to $E\sim 28$ GPa and $\nu\sim 0.3$ (Sanahuja, 2010).

We performed measurements on large scale gypsum samples (40x40x160 mm prisms) on which Young's moduli were investigated by uniaxial compression and by the resonant method. Both measurements gave similar values of the mean Young's modulus: $E\sim 28.6\pm 0.2$ GPa in compression tests and $E\sim 26.6\pm 0.4$ GPa, $\nu=0.29\pm 0.008$ in the resonant method, respectively. Thus, good agreement with the homogenized result on our samples ($E\sim 29.46$ GPa, $\nu=0.31$) was achieved.

9. Conclusions

Effective elastic properties of selected heterogeneous structural materials were studied by nanoindentation and methods of micromechanics. Cement paste and gypsum (α -hemihydrate) were in focus but the methodology described in this chapter can be easily adopted for other heterogeneous materials, e.g. for high-performance concretes and mortars (Sorelli et al., 2008; Němeček et al., 2011b), alkali-activated materials (Němeček et al., 2011c) or for metal alloys (Němeček et al., 2011a).

Firstly, nanoindentation was utilized for the assessment of elastic parameters of small material volumes. The size of individual indents was kept small enough ($h\sim 200$ -500 nm) to represent individual phase behaviour. The mechanical response was received from the volume $\sim 0.7^3$ - 1.5^3 μm^3 . As an unavoidable fact, intrinsic porosity of the constituents was included in nanoindentation results.

Complicated microstructures of the studied heterogeneous structural materials and impossible ex-situ preparation of individual material constituents lead to the use of statistical grid indentation to cover the response from all phases. Elastic constants of the basic constituents have been derived and further used in multi-scale models to receive effective composite properties within the RVE.

Deconvolution technique has proven to be an efficient tool for the separation of distinct phases in cement paste. On the other hand, local anisotropy of the polycrystalline gypsum matrix was not assessed and effective (average) matrix properties have been directly derived from the grid nanoindentation as mean values.

Effective RVE properties were successfully determined with analytical schemes (Mori-Tanaka, self-consistent) and verified with numerical FFT-based method. The performance of both approaches was in good agreement for the tested materials. Comparison with macroscopic experimental data also showed good correlation with the predicted values and validated the presented methodology.

Author details

Jiří Němeček

Czech Technical University in Prague, Faculty of Civil Engineering, Department of Mechanics, Czech Republic

Acknowledgement

Support of the Czech Science Foundation (P105/12/0824) is gratefully acknowledged.

10. References

- Beaudoin, J.J.; Raki, L.; Alizadeh, R. & Mitchell, L. (2010). Dimensional change and elastic behavior of layered silicates and Portland, cement paste, *Cement & Concrete Composites* 32, pp. 25–33.
- Bentz, D.P. & Garboczi, E.J. (1999). Computer Modelling of Interfacial Transition Zone: Microstructure and Properties, *Engineering and Transport Properties of the Interfacial Transition Zone in Cementitious Composites*, Rilem Report No. 20, RILEM Publ. s.a.r.l., Cachan, France, Part 5, Chapter 20, pp. 349-385.
- Borodich, F.M.; Keer, L.M. & Korach, C.J. (2003). Analytical study of fundamental nanoindentation test relations for indenters of non-ideal shapes, *Nanotechnology* 14 (7), pp. 803-808.
- Constantinides, G. & Ulm, F.-J. (2004). The effect of two types of C–S–H on the elasticity of cement-based materials: results from nanoindentation and micromechanical modeling, *Cement and Concrete Research* 34 (1), pp. 67–80.
- Constantinides, G. & Ulm, F.-J. (2007). The nanogranular nature of C–S–H, *Journal of the Mechanics and Physics of Solids* 55, pp. 64–90.
- Constantinides, G.; Chandran, F.R.; Ulm, F.-J. & Vliet, K.V. (2006). Grid indentation analysis of composite microstructure and mechanics: Principles and validation, *Materials Science and Engineering: A*, 430 (1-2), pp. 189-202.

- Drugan, W.R. & Willis, J.R. (1996). A micromechanics-based nonlocal constitutive equation and estimates of representative volume element size for elastic composites, *Journal of the Mechanics and Physics of Solids* 44 (4), pp. 497–524.
- Durst, K.; Göken, M. & Vehoff, H. (2004). Finite element study for nanoindentation measurements on two-phase materials, *J Mater. Res.* 19 , pp. 85–93.
- Eshelby, J.D. (1957). The determination of the elastic field of an ellipsoidal inclusion and related problem, *Proc. Roy. Soc. London A* 241, pp. 376–396.
- Fischer-Cripps, A.C. (2002). *Nanoindentation*, Springer Verlag, ISBN 0-387-95394-9.
- Gao, H.J.; Chiu, C.H. & Lee, J. (1992). Elastic contact versus indentation modeling of multi-layered materials, *International Journal of Solids and Structures* 29 (20), pp. 2471–2492.
- Hashin, Z. (1983). Analysis of composite materials - a survey. *ASME J. Appl. Mech.* 50, pp. 481–505.
- Hausuhl, S. (1960). Elastische und thermoelastische Eigenschaften von $\text{CaSO}_4 \cdot 2\text{H}_2\text{O}$ (Gips), *Zeitschrift für Kristallographie* 122, pp. 311–314.
- Hill, R. (1963). Elastic properties of reinforced solids - Some theoretical principles. *Journal of the Mechanics and Physics of Solids* 11, pp. 357–372.
- Hill, R. (1965). Continuum micro-mechanics of elastoplastic polycrystals. *Journal of the Mechanics and Physics of Solids* 13, pp. 89–101.
- Hughes, J.J. & Trtik, P. (2004). Micro-mechanical properties of cement paste measured by depth-sensing nanoindentation: a preliminary correlation of physical properties with phase type, *Mater Charact* 53, pp. 223–31.
- Jiroušek, O.; Janděšek, I. & Vavřík, D. (2011a). Evaluation of strain field in microstructures using micro-CT and digital volume correlation, *Journal of Instrumentation* 6 (1), art. no. C01039.
- Jiroušek, O.; Němeček, J.; Kytýř, D.; Kunecký, J.; Zlámal, P. & Doktor, T. (2011b). Nanoindentation of trabecular bone-comparison with uniaxial testing of single trabecula, *Chemické Listy* 105 (17), pp. s668-s671.
- Meille, S. & Garboczi, E. J. (2001). Linear elastic properties of 2D and 3D models of porous materials made from elongated objects. *Modell. Simul. Mater. Sci. Eng.* 9(5), pp. 371–390.
- Michel, J.C.; Moulinec, H. & Suquet, P. (1999). Effective properties of composite materials with periodic microstructure: a computational approach, *Comput. Methods Appl. Mech. Engrg.* 172, pp. 109–143.
- Mori, T. & Tanaka, K. (1973). Average stress in matrix and average elastic energy of materials with misfitting inclusions, *Acta Metallurgica* 21 (5), pp. 571–574.
- Moulinec, H. & Suquet, P. (1994). A fast numerical method for computing the linear and nonlinear properties of composites, *Comptes-Rendus de l'Académie des Sciences série II* 318, pp. 1417–1423.
- Moulinec, H. & Suquet, P. (1998). A numerical method for computing the overall response of nonlinear composites with complex microstructure, *Computer Methods in Applied Mechanics and Engineering* 157 (1–2), pp. 69–94.
- Němeček, J. (2009). Creep effects in nanoindentation of hydrated phases of cement pastes, *Materials Characterization* 60 (9), pp. 1028–1034.
- Němeček, J.; Králík, V.; Vondřejc, J. & Němečková, J. (2011a). Identification of micromechanical properties on metal foams using nanoindentation, *Proceedings of the Thirteenth International Conference on Civil, Structural and Environmental Engineering Computing* [CD-ROM]. Edinburgh: Civil-Comp Press, 2011, pp. 1–12. ISBN 978-1-905088-46-1.

- Němeček, J.; Lehmann, C. & Fontana, P. (2011b). Nanoindentation on Ultra High Performance Concrete System, *Chemické Listy* 105 (17), pp. 656-659.
- Němeček, J.; Šmilauer, V. & Kopecký, L. (2011c). Nanoindentation characteristics of alkali-activated aluminosilicate materials, *Cement and Concrete Composites* 33 (2), pp. 163-170.
- Oliver, W. & Pharr, G.M. (1992). An improved technique for determining hardness and elastic modulus using load and displacement sensing indentation experiments, *J. Mater. Res.* 7 (6), pp. 1564–1583, 1992.
- Randall, N.X. (2009). Mechanical Properties of Cementitious Materials, *CSM Instruments Application Bulletin* No.29, available from: <http://www.csm-instruments.com/>
- Sanahuja, J.; Dormieux, L.; Meille, S.; Hellmich, C. & Fritsch, A. (2010). Micromechanical Explanation of Elasticity and Strength of Gypsum: From Elongated Anisotropic Crystals to Isotropic Porous Polycrystals, *Journal of Engineering Mechanics* 136 (2), pp. 239-253.
- Saranen, J., Vainikko, G. (2002), *Periodic Integral and Pseudodifferential Equations with Numerical Approximation*, Springer, Berlin.
- Singh, N.B. & Middendorf, B. (2007). Calcium sulphate hemihydrate hydration leading to gypsum crystallization, *Progress in Crystal Growth and Characterization of Materials* 53 (1), pp. 57–77.
- Sorelli, L.; Constantinides, G.; Ulm, F.-J. & Toutlemonde, F. (2008). The nano-mechanical signature of Ultra High Performance Concrete by statistical nanoindentation techniques, *Cement and Concrete Research* 38, pp.1447–1456.
- Swadener J.G & Pharr, G.M. (2001). Indentation of elastically anisotropic half-spaces by cones and parabolae of revolution, *Phil. Mag. A* 81 (2), pp. 447-466.
- Šmilauer, V.; Hlaváček, P.; Škvára, F.; Šulc, R.; Kopecký, L. & Němeček, J. (2011). Micromechanical multiscale model for alkali activation of fly ash and metakaolin, *Journal of Materials Science* 46 (20), pp. 6545-6555.
- Taylor, H.F.W. (2003). *Cement Chemistry, Second Edition*, Thomas Telford, ISBN 0-7277-2592-0.
- Tennis, P.D. & Jennings, H.M. (2000). A Model for Two Types of C-S-H in the Microstructure of Portland Cement Pastes, *Cement and Concrete Research* 30 (6), pp. 855-863.
- Tesárek, P. & Němeček, J. (2011). Microstructural and Micromechanical Study of Gypsum, *Chemické Listy* 105 (17), pp. 852-853.
- Thomas, J.J.; Jennings, H.M. & Allen, A.J. (1998). The Surface Area of Cement Paste as Measured by Neutron Scattering – Evidence for Two C-S-H Morphologies, *Cement and Concrete Research* 28 (6), pp. 897-905.
- Ulm, F.-J.; Vandamme, M.; Bobko, C. & Ortega, J.A. (2007). Statistical Indentation Techniques for Hydrated Nanocomposites: Concrete, Bone, and Shale, *J. Am. Ceram. Soc.* 90 (9), pp. 2677–2692.
- Vlassak, J.J.; Ciavarella, M.; Barber, J.R. & Wang, X. (2003). The indentation modulus of elastically anisotropic materials for indenters of arbitrary shape, *Journal of the Mechanics and Physics of Solids* 51, pp. 1701 – 1721.
- Zaoui, A. (2002). Continuum Micromechanics: Survey, *Journal of Engineering Mechanics* 128 (8), pp. 808–816.
- Zeman, J.; Vondřejc, J.; Novák, J. & Marek, I. (2010). Accelerating a FFT-based solver for numerical homogenization of periodic media by conjugate gradients, *Journal of Computational Physics* 229(21), pp. 8065-8071.